A. NORMAN JETTE and C. BRENT BARGERON

THEORY OF ELECTRON CURRENT IMAGE DIFFRACTION FROM CRYSTAL SURFACES AT LOW ENERGIES

Images obtained by rastering an electron beam across the surface of a single crystal while measuring the current absorbed by the specimen and displaying it synchronously as a function of beam azimuthal and polar angles on a cathode-ray tube reveal diffraction patterns characteristic of the symmetry of atomic positions on and near the crystal surface. Information about crystal structure and electron–surface interactions can be obtained by comparing these images with theoretical computations.

INTRODUCTION

Current-image diffraction (CID) was discovered in 1982 in APL's Milton S. Eisenhower Research Center.[1] This phenomenon has been described in previous articles in the *Technical Digest*.[2,3] Briefly, an electron beam is rastered across the surface of a meticulously polished and cleaned single crystal of a metal or semiconductor in an ultrahigh vacuum ($\sim 10^{-9}$ to 10^{-10} torr). The current absorbed by this crystal is synchronously measured as a function of beam azimuthal and polar angles and displayed on a cathode-ray tube. Changes in contrast reveal diffraction patterns caused by variations in total reflectivity of the crystal surface with the angle of incidence of the electron beam (Fig. 1). Conservation of electron flux results in the initial electron beam current equaling the sum of the current absorbed by the crystal plus that reflected or emitted from the surface. This article addresses calculation of the reflectivity as a function of electron beam energy and angle of incidence.
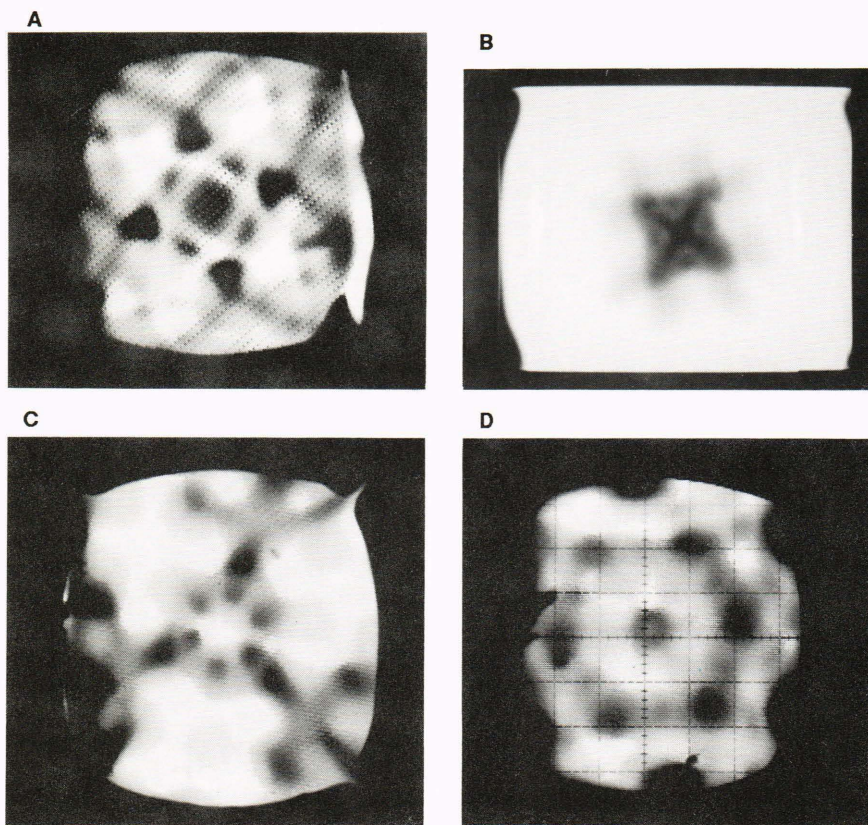
Figure 1. Experimental current image diffraction pattern. The planar Miller (hkl) indices for these surfaces are illustrated in Ref. 2. **A.** The (001) surface of aluminum taken at a primary beam energy of E_p = 21 eV with respect to the vacuum. **B.** The (001) surface of aluminum with E_p = 162 eV. **C.** The (111) surface of aluminum with E_p = 21 eV. **D.** The basal plane of titanium at E_p = 20 eV.

The theory of CID images is closely allied with that of low-energy electron diffraction (LEED), a theory that was developed in the late 1960s and early 1970s.[4] With LEED, the important quantity is the intensity of individual beams that are elastically backscattered (diffracted) from the crystal and often displayed as spots on a hemispherical fluorescent screen,[2] with inelastically scattered electrons prevented from reaching the screen by retarding grids. Comparing the intensity of LEED beams as a function of primary beam energy with the experimental results allows the extraction of useful structural information about the crystal surface. With CID, on the other hand, the total elastically diffracted component is of interest; that is, the sum of all the LEED beams that can backscatter from the crystal at a particular energy and angle of incidence determines the total elastic component of surface reflectivity. Structural information on symmetry and atomic position is derived from CID images by comparison with theoretical calculations of the elastic component of reflectivity.

ION–CORE SCATTERING

A characteristic length of the incident electron beam, termed the coherence length, is the distance on the crystal surface within which all atoms will experience radiation of equal amplitude and phase. The coherence length at LEED energies (10 to 1000 eV) is on the order of 500 Å,[4] a distance that encompasses about 200 surface unit cells, depending on the crystal; thus, the incident electron beam can be taken as an infinitely wide beam on the microscopic scale, described by a plane wave. Mathematically, the incident beam of amplitude A and position $\mathbf{r}$ can be written as $A \exp(i\mathbf{k}_0 \cdot \mathbf{r})$ with energy $E = \hbar^2 |\mathbf{k}_0|^2 / 2m_e$, where $\hbar$ is Planck's constant divided by 2π, m_e is the electron mass, and $|\mathbf{k}_0|$ is $2\pi/\lambda_0$, with λ_0 the electron wavelength outside the crystal. A schematic of an electron beam taken as a plane wave incident in the normal direction on a crystal surface is shown in Figure 2. Localized ion cores strongly elastically scatter the electrons, whereas delocalized conduction or valence electrons are primarily responsible for the inelastic processes that diminish the amplitude of the incident beam penetrating into the bulk crystal, where it eventually decays. The crystal is therefore modeled as a periodic array of spherically symmetric potentials located at atomic positions that describe the tightly bound core electrons of the crystal atoms. These potentials are immersed in a complex potential termed the inner, or optical, potential. The real part of the inner potential is taken as a constant and accounts for the contribution of the delocalized electrons to the elastic scattering of the electron probe; this interaction is weak. The imaginary part is dependent on the incident electron's energy and takes into account the inelastic scattering processes that attenuate the amplitude of the electron beam.

The calculation first proceeds by considering the scattering of an incident electron by an isolated spherically symmetric ion core;[4] that is, the Schrödinger equation
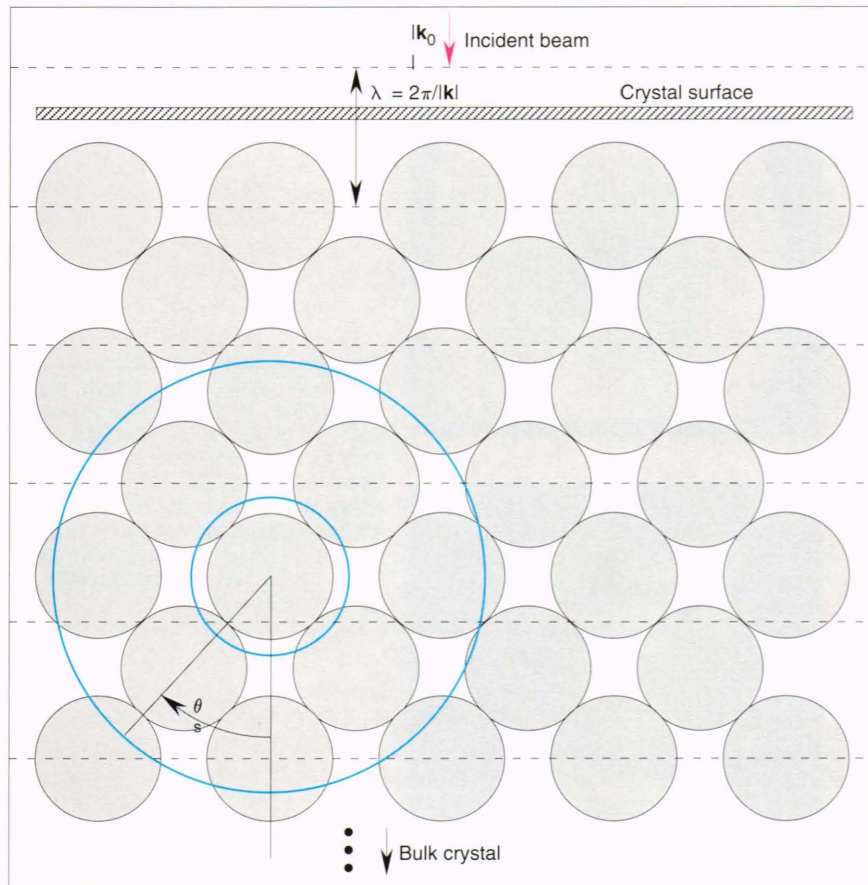
Figure 2. Schematic of an electron beam of energy E taken as a plane wave incident in the normal direction to the crystal surface. The dashed lines indicate the wavelength of the electron beam in the crystal "inner" potential $V_0 (\lambda = 2\pi \sqrt{2E - 2V_0})$. One scattering event is drawn where scattered waves radiate from the ion core (scattering center), with amplitudes dependent on the scattering angle θ_s.

must be solved for the many-electron system that consists of the tightly bound core states, $\psi_n(\mathbf{r}_i, \mathbf{s}_i)$ for electron i in quantum state n, and the wave function of the incident and scattered electrons, $\phi(\mathbf{r}_j, \mathbf{s}_j)$, where $\mathbf{r}_j$ is an electron-position coordinate and $\mathbf{s}_j$ is the spin coordinate of electron j. This many-electron function satisfies

$$\mathbf{H}\Phi = E_t\Phi , \qquad (1)$$

where

$$\Phi(\mathbf{r}_1, \mathbf{s}_1 \ldots \mathbf{r}_{N+1}, \mathbf{s}_{N+1}) = \sum_P (-1)^P \phi(\mathbf{r}_1, \mathbf{s}_1)$$

$$\times \psi_1(\mathbf{r}_2, \mathbf{s}_2) \ldots \psi_N(\mathbf{r}_{N+1}, \mathbf{s}_{N+1})$$

$$(2a)$$

is the many-electron wave function for the N core electrons plus the incident or scattered electron, and

$$\mathbf{H} = \sum_{j=1}^{N+1} \left[-\frac{\hbar^2}{2m}\nabla_j^2 - \frac{Ze^2}{|\mathbf{r}_j|} + V_s(\mathbf{r}_j) + \sum_{i=j+1}^{N+1} \frac{e^2}{|\mathbf{r}_i - \mathbf{r}_j|} \right]$$

$$(2b)$$

is the many-electron Hamiltonian. Here m and e are the electron mass and charge, respectively. E_t is the total energy of the system, including all the core levels and incident electron probe. The sum in Equation 2a is over all permutations P of electron coordinates, where an order derived from the initial order by an even permutation of two electrons results in a positive sign, and an odd exchange contributes negatively. This wave function satisfies the condition that a many-electron wave function must be antisymmetric with respect to the exchange of any two particles. The Hamiltonian (Eq. 2b) is a sum over the single-particle kinetic energy operators and the electrostatic potentials describing the interaction of an electron with the nucleus of charge Z and the electrostatic repulsion between electrons. In this equation, $V_s(\mathbf{r}_j)$ is the potential due to screening by the delocalized electrons and is constructed so as to make the ion-core region electrically neutral. Thus, when the electron probe is external to the ion core, it is in a field-free region except for the constant term of the inner potential.

At first sight, the solution of Equation 1 seems formidable, but there is much information about the system that can be used to advantage. The total energy E_t is the sum of the incident electron energy and the total energy of the core states E_{tc}. Because the energy (20 to 1000 eV) of the incident electron is much higher than the conduction or valence electrons (3 to 5 eV), the screening charge has relatively less effect on the LEED or CID electron than on the conduction electrons. Thus, the main effect of the screening electrons is to ensure charge neutrality, and most reasonable approximations of the screening potential in the ion-core region will yield satisfactory results.[4] The core electrons are also tightly bound and not

easily polarized by the incident electron. Thus, we can take for the core states the known solutions for the free atom, and the functions $\psi_n(\mathbf{r}_i, \mathbf{s}_i)$ are elements of a complete orthonormal set, which can be exploited to obtain an equation for $\phi(\mathbf{r}, \mathbf{s})$ alone. The CID electron wave function can be decomposed into partial waves centered on the ion core

$$\phi(\mathbf{r}, \mathbf{s}) = \sum_{l,m} a_{l,m}\sigma_s\phi_l(|\mathbf{r}|)Y_{l,m}(\theta, \phi) , \qquad (3)$$

where $Y_{l,m}(\theta, \phi)$ is a spherical harmonic, $a_{l,m}$ is the amplitude of the partial wave l,m, and σ_s is a spin function. Because the ion core is spherically symmetric, it cannot absorb angular momentum, and each partial wave component l and m is consequently conserved. The partial waves ϕ_l behave independently and satisfy

$$-\frac{\hbar^2}{2m}\left\{ \frac{1}{r^2}\frac{d}{dr}\left[r^2\frac{d\phi_l(r)}{dr} \right] - \frac{l(l+1)}{r^2}\phi_l(r) \right\}$$

$$+ \left[V_s(r) - \frac{Ze^2}{r} + \sum_{n,s} e^2 \int \frac{|\psi_n(\mathbf{r}', \mathbf{s})|^2}{|\mathbf{r} - \mathbf{r}'|} d^3\mathbf{r} \right]\phi_l(r)$$

$$+ \int_0^\infty V_{ex}^l(r, r')\phi_l(r')r'^2\, dr' = E\phi_l(r) \qquad (4a)$$

inside the ion core and

$$-\frac{\hbar^2}{2m}\left[\frac{1}{r^2}\frac{d}{dr}\left(r^2\frac{d\phi_l}{dr} \right) - \frac{l(l+1)}{r^2}\phi_l(r) \right] = E\phi_l(r)$$

$$(4b)$$

outside this sphere. In Equation 4a, V_{ex}^l is a nonlocal operator called the exchange potential and is a direct consequence of the antisymmetric property of the many-electron wave function (Eq. 2a).

Solutions to Equation 4b in the region exterior to the ion core can be written in terms of unscattered, $\phi_l^{(0)}$, and scattered, $\phi_l^{(s)}$, constituents, namely,

$$\phi_l = \phi_l^{(0)}(r) + \phi_l^{(s)}(r) , \qquad (5a)$$

where

$$\phi_l^{(0)} = \beta_l[h_l^{(1)} + h_l^{(2)}] = 2\beta_l j_l , \qquad (5b)$$

and

$$\phi_l^{(s)} = \beta_l[\exp(2i\delta_l) - 1]\, h_l^{(2)} . \qquad (5c)$$

In these equations, $h_l^{(1)}$ and $h_l^{(2)}$ are spherical Hankel functions of the first and second kind of order l.[5]

In the limit of large argument r, $h_l^{(1)}$ behaves as an outgoing wave, whereas $h_l^{(2)}$ acts as an incoming wave. The term j_l is the spherical Bessel function of order l, β_l is the amplitude of the incoming wave, and δ_l is a phase shift for angular momentum l. The incoming plane wave can be resolved into spherical components using the identity

$$\exp(i\mathbf{k} \cdot \mathbf{r}) = \sum_{l=0}^{\infty} \sum_{m=-l}^{l} 4\pi i^l j_l(|\mathbf{k}|r) \, Y_{lm}^{*}[\Omega(\mathbf{k})] Y_{lm}[\Omega(\mathbf{r})] \, , \tag{6}$$

where Ω denotes both polar and azimuthal angles of its vector argument and the asterisk (*) indicates complex conjugation. Direct comparison of Equation 6 with the solution to the Schrödinger equation in the region external to the ion cores (Eq. 5) establishes the amplitudes β_l. The total scattered component of Equation 3 is consequently

$$\phi^{(s)}(\mathbf{r}) = \sum_{l} i^l \tfrac{1}{2} [\exp(2i\delta_l) - 1] h_l^{(1)}(|\mathbf{k}|r)$$

$$\times (2l + 1) P_l(\cos \theta^{(s)}) \, , \tag{7}$$

where $\theta^{(s)}$ is the angle between $\mathbf{r}$ and $\mathbf{k}$, or the scattering angle, and P_l is a Legendre polynomial.

The phase shifts are determined by solving for the logarithmic derivative

$$L_l(R) = \frac{\phi_l'(R)}{\phi_l(R)} \, , \tag{8}$$

where $\phi_l(R)$ and $\phi_l'(R)$ are determined numerically from Equation 4a. Because the solutions exterior to the ion core must match at the core boundary R, this condition results in

$$\exp(2i\delta_l) = \frac{L_l h_l^{(2)} - h_l^{(2)\prime}}{h_l^{(1)\prime} - L_l h_l^{(1)}} \tag{9}$$

for the phase shifts, where a prime denotes differentiation with respect to r. Although the sum in Equation 7 is over all values of l in practice, only a finite number, increasing with primary beam energy, are required to obtain convergence. For example, at $E = 50$ eV, only values of l up to 4 are significant.[4] Once accurate solutions of the scattered wave (Eq. 7) are obtained for an ion-core potential, the ion cores are assembled into periodic structures that are representative of the crystal and immersed in the complex optical potential.

MUFFIN–TIN POTENTIAL

The real part of the inner potential, V_0 in Figure 3, is roughly the sum of the work function (energy required to remove an electron from the crystal) and the Fermi energy (energy of the highest occupied conduction-band electron at temperature $T = 0$ K). The imaginary part of the inner potential is dependent on the energy of the primary beam and represents the losses suffered by the beam due to inelastic processes. The imaginary part of this potential makes elastic, low-energy electron scattering surface-specific, because the beam attenuates as it penetrates into the bulk crystal; consequently, the elastically backscattered electrons sample only the first few layers of atoms. In Figure 3A the crystal surface is at $z = 0$, and the transition from vacuum to crystal surface is along the negative z-axis. The potential in this region is referred to as the surface barrier, which can be thought of as being caused by an image charge and is potentially observed as fine structure in the current-image diffraction (CID) images near the evanescent condition for the emergence of a new electron beam.[3] The resemblance of the potential to a muffin tin, accounting for its name, is evident in Figure 3B.

To the right of the origin in Figure 3A is the potential inside the crystal where the symmetrically arranged ion-core potentials are coulomb-like, with regions of constant potential between them, the so-called muffin-tin potential depicted three-dimensionally in Figure 3B. Unlike X rays, where scattering per collision is weak, electron scattering is strong, and multiple scattering events must be taken into account to obtain accurate intensities of the backscattered electrons; this feature makes low-energy electron scattering computationally intensive. Indeed, the calculation is made tractable only by the periodicity of the ion-core scattering centers. The wave func-
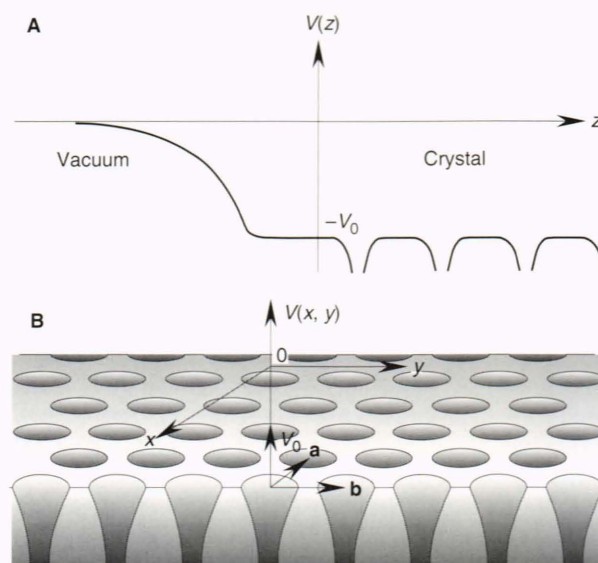
Figure 3. Muffin-tin potential for a single crystal. **A.** The surface is at $z = 0$, and the approach to the vacuum is along $z < 0$. **B.** Three-dimensional perspective where the surface unit cell is given by **a** and **b**. (V_0 = real part of inner potential.)

tions at the various scattering centers have distinct phase relationships because of this periodicity.

MULTIPLE SCATTERING

Multiple scattering effects can be calculated in many ways, but only two approaches are described here. Both approaches proceed by dividing the crystal into planes or layers of atoms parallel to the crystal surface, with the division dependent on the complexity of the structure. The transmission and reflectivity of a plane or layer of atoms are calculated for incident and scattered beams exterior to the plane or layer. The number of diffracted beams is determined by the primary beam energy, and their direction is fixed by crystal symmetry. The multiple scattering of the ion cores is treated self-consistently. For example, the scattering of an ion core centered at the origin of the surface unit cell is calculated for the incident plane wave, thereby determining the scattering of all other ion cores in other unit cells in equivalent positions, as they are related to each other only by differences in phase. The scattered waves from all the other ion cores are then treated as incident waves on the original core at the origin; that is, the scattering of the incident plane wave is corrected for multiple scattering effects by adding to the incident wave all the waves scattered from other ion cores. The summation over other ion cores usually converges rapidly owing to absorption.

The layers can be complicated entities involving several planes of atoms in which each plane of atoms has its ion cores in the same plane. For simplicity, we shall consider a single plane of atoms to constitute a structural unit, termed the surface unit cell, that replicates the plane by translations of lattice vectors, $\mathbf{R}_j$,

$$\mathbf{R}_j = n\mathbf{a} + m\mathbf{b} \ , \tag{10}$$

where n and m are integers, and $\mathbf{a}$ and $\mathbf{b}$ are basis vectors in the plane for the basic structural unit (Fig. 3B). Both $\mathbf{a}$ and $\mathbf{b}$ are determined by the symmetry of the positions of the atoms that make up the plane. The kth atom in the jth unit is denoted

$$\mathbf{R}_{jk} = \mathbf{R}_j + \mathbf{r}_k \ , \tag{11}$$

where $\mathbf{r}_k$ is a vector from the origin of the unit cell to the kth atom within it. To calculate scattering by this plane, consider the incident plane waves from the left of the plane (superscript plus signs) of the expression

$$\sum_{\mathbf{g}} U_{\mathbf{g}}^+ \exp(i\,\mathbf{K}_{\mathbf{g}}^+ \cdot \mathbf{r}) \ ,$$

where the sum is over vectors of the reciprocal lattice $\mathbf{g}$, which satisfy

$$\mathbf{g} \cdot \mathbf{a} = 2\pi i$$

$$\mathbf{g} \cdot \mathbf{b} = 2\pi j \ , \tag{12}$$

where i and j are integers. The term $U_{\mathbf{g}}^+$ is the amplitude of the gth beam, and $\mathbf{K}_{\mathbf{g}}^\pm$ is the complex wave vector or momentum of the beam $\mathbf{g}$ incident from the left of the plane (positive superscript) or right of the plane (negative superscript). Here, atomic units are being used for notational convenience ($\hbar^2 = m_e = e^2 = 1$). In these atomic units, the unit of energy is the Rydberg (27.2 eV), and the unit of distance is the Bohr radius (0.529 Å). The imaginary component of $\mathbf{K}_{\mathbf{g}}^\pm$ attenuates the beam until it diminishes. The absolute values of these wave vectors are

$$\kappa \equiv |\mathbf{K}_{\mathbf{g}}^\pm| \approx (2E - 2V_{0r})^{1/2} \ , \tag{13}$$

where V_{0r} is the real component of the complex optical potential. The plane waves can be reexpressed in terms of spherical waves centered on the kth atom in the unit cell at the origin, using the identity of Equation 6. Proceeding in much the same way as for a single ion core (Eq. 7), the scattered flux for many beams can be found by

$$\psi_s^{(0)} = \sum_{lmjk} A_{lmk}^{(0)} \ \tfrac{1}{2} \{\exp[2i\delta_l(k)] - 1\} \ h_l^{(1)} (\kappa|\mathbf{r} - \mathbf{R}_{jk}|)$$

$$\times \exp[i\mathbf{k}_{0\parallel} \cdot (\mathbf{R}_{jk} - \mathbf{R}_{0k})] Y_{lm}[\Omega(\mathbf{r} - \mathbf{R}_{jk})] \ , \tag{14}$$

where $\Omega(\mathbf{r} - \mathbf{R}_{jk})$ stands for the angular coordinates of the vector $(\mathbf{r} - \mathbf{R}_{jk})$ and $\mathbf{k}_{0\parallel}$ is the component of the incident wave vector parallel to the crystal surface. In deriving Equation 14, use was made of the identity

$$A_{lmk}^{(0)}(j\text{th cell}) = A_{lmk}^{(0)}(0\text{th cell}) \exp[i\mathbf{k}_{0\parallel} \cdot \mathbf{R}_j] \ , \tag{15}$$

or the wave function at $\mathbf{R}_{jk}$ is identical to the wave function at $\mathbf{R}_{0k}$ except for a phase factor.

As it stands, $\psi_s^{(0)}$ includes scattering events of the incident beams to atoms in the plane and does not include waves scattered from other ion cores incident on atoms within the plane. The total amplitude, including scattering from other ion cores on the kth ion core in the unit cell at the origin, is

$$A_{lmk} = A_{lmk}^{(0)} + A_{lmk}^{(s)} \ , \tag{16}$$

where $A_{lmk}^{(s)}$ is the amplitude scattered from other ion cores in the plane. The term $A_{lmk}^{(s)}$ depends on A_{lmk} and consequently must be determined self-consistently. The amplitude of the wave at the kth atom in the jth unit cell is related to that of the kth atom in the 0th unit cell by just a phase factor (Eq. 15). By using this property and an expansion theorem for the product of spherical Hankel functions and spherical harmonics, an equation can be derived for the total scattered wave by the plane of atoms, including multiple scattering from all ion cores in addition to the incident beams.[4]

Because these equations are rather complex, only the results will be repeated here, and the interested reader is referred to Pendry for the details.[4] The total amplitudes $V_\mathbf{g}^\pm$, including waves that scattered and waves that passed through the plane without scattering, can be written as

$$V_{\mathbf{g}'}^+ = \sum_\mathbf{g} (I_{\mathbf{g}'\mathbf{g}} + M_{\mathbf{g}'\mathbf{g}}^{++})U_\mathbf{g}^+ + M_{\mathbf{g}'\mathbf{g}}^{+-} U_\mathbf{g}^- \qquad (17a)$$

and

$$V_{\mathbf{g}'}^- = \sum_\mathbf{g} M_{\mathbf{g}'\mathbf{g}}^{-+} U_\mathbf{g}^+ + (I_{\mathbf{g}'\mathbf{g}} + M_{\mathbf{g}'\mathbf{g}}^{--})U_\mathbf{g}^- , \qquad (17b)$$

where $I_{\mathbf{g}'\mathbf{g}}$ are elements of the identity matrix and $U_\mathbf{g}^\pm$ the amplitudes of the incident plane waves of wave vector $\mathbf{K_g}$ incident from the left of the plane (positive superscript) and from the right of the plane (negative superscript). To grasp the complexity of the solution, elements of the scattering matrix are explicitly

$$M_{\mathbf{g}'\mathbf{g}}^{\pm\pm} = \frac{8\pi^2 i}{|\mathbf{K}_\mathbf{g}^\pm| A K_{\mathbf{g}'z}^+} \sum_{\substack{l'm'k' \\ lmk}} \exp(i\mathbf{K}_\mathbf{g}^\pm \cdot \mathbf{r}_k - i\mathbf{K}_{\mathbf{g}'}^\pm \cdot \mathbf{r}_{k'})$$

$$\times \{i^l(-1)^m Y_{l-m}[\Omega(\mathbf{K}_\mathbf{g}^\pm)]\}[1 - X]^{-1}_{lmk,l'm'k'}$$

$$\times \{i^{-l'} Y_{l'm'}[\Omega(\mathbf{K}_{\mathbf{g}'}^\pm)]\}$$

$$\times \exp[i\delta_{l'}(k')]\sin[\delta_{l'}(k')] , \qquad (18)$$

where A is the area of a surface unit cell, and X is a matrix with elements given by

$$X_{lmk,l''m''s} = -\exp[i\delta_l(k)]\sin[\delta_l(k)]$$

$$\times \sum_{l'm'} 4\pi\kappa^{-1}(-1)^{(l''-l-l')/2}(-1)^{m''}$$

$$\times \int Y_{lm}(\Omega)Y_{l'm'}(\Omega)_{l''-m''}(\Omega) \, d\Omega$$

$$\times \left[\frac{\kappa i \delta_{m'0}\delta_{l0}}{\sqrt{4\pi}} + D_{l'm'}(ks)\right] . \qquad (19)$$

Note that in these equations δ_l is the traditional notation for a phase shift; $\delta_{i,j}$ is the Kronecker delta function ($\delta_{i,j} = 1$ if $i = j$ and $\delta_{i,j} = 0$ for $i \neq j$). In Equation 19, $D_{l'm'}(ks)$ involves a sum over all the unit cells j, namely,

$$D_{l'm'}(ks) = \frac{\kappa i}{\sqrt{4\pi}}\, \delta_{m'0}\, \delta_{l'0} - i\kappa(-1)^{l'+m'}$$

$$\times \sum_j{}' h_{l'}^{(1)}(\kappa|\mathbf{R}_{0s} - \mathbf{R}_{jk}|)Y_{l'-m'}[\Omega(\mathbf{R}_{0s} - \mathbf{R}_{jk})]$$

$$\times \exp(i\mathbf{k}_{0\parallel} \cdot \mathbf{R}_j) , \qquad (20)$$

where the prime on the sum denotes the exclusion of the 0th unit cell from the sum. The total scattered wave function in terms of the amplitudes (Eq. 17) is

$$\psi_s^{(0)\pm} = \sum_{\mathbf{g}'} V_{\mathbf{g}'}^\pm \exp(i\mathbf{K}_{\mathbf{g}'}^\pm \cdot \mathbf{r})$$

to the left and right sides of the plane.

Although in our sketch of the theory just described we have restricted ourselves for simplicity to a single plane of atoms, Equation 18 is more general; that is, $\mathbf{r}_k$ may also have a z component, and the single plane can, in fact, be a layer of atoms. This should usually be avoided, because the dimensions of X depend on the number of ion cores in the unit cell, which results in computer inefficiencies for many different ion cores in assembling X and determining the inverse of $(1 - X)$. For a single plane of atoms of spherical symmetry, the scattering matrix is independent of the side of the plane on which the plane waves are incident, that is, $M^{+-} = M^{-+}$ and $M^{++} = M^{--}$. The complexity of a low-energy electron diffraction (LEED) or a current-image diffraction (CID) calculation is caused in part by the profusion of beams that results from a plane wave striking a plane or layer of atoms, much akin to plucking a clamped string and analyzing the resulting motion in terms of the string's normal modes. The number of these beams is limited only by the energy because, for large $\mathbf{g}$, the waves become evanescent and die away. For the CID calculations, once the scattering matrix for the plane or layer of atoms is determined, the layer-doubling or renormalized forward-scattering theory is used to complete the calculation for the total elastic component of the reflectivity.

The layer-doubling scheme for calculation proceeds by taking the single layer or plane and doubling it at the crystal layer separation. The transmission and reflectivity computations are then repeated for the transmitted and reflected beams external to the doubled layer. This composite layer is again doubled, and the process is repeated. Eight identical layers or planes are usually sufficient to approximate the semi-infinite crystal. This is the method of choice for low primary-beam energies such as those used to probe surface potential effects.[4,6]

Another method used to obtain CID images is the renormalized forward-scattering perturbation method.[4] Perturbation theories in general fail for electron scattering at low energies, primarily because of the strong electron–ion-core scattering at these energies. Pendry[4] developed a perturbation approach that does succeed, however, and achieves more computer economy than

260

other methods. This method exploits the fact that only the forward-scattering events are strong, $\theta_s < 90°$. Consequently, forward scattering is treated to all orders of scattering. This method proceeds by considering all scattering events between layers 0 and j. That is, in zero order, no scattering of the incident beam occurs as it passes through all the intervening layers and emerges from layer j; in first order, only one scattering event occurs between the surface and the beams emerging from layer j. This single-scattering event must be summed over all the layers, however. After the zero-order and first-order terms are found, the second-order, third-order, and so on, are considered until, finally, forward-scattering occurs from every intervening layer, including the layer j. This sequence can be summed to give an exact expression for the forward-scattering amplitude; thus, the strong forward scattering is treated exactly. Backscattering is dealt with by using the perturbation theory, a method that greatly reduces the computational time and is the method of choice for higher primary-beam energies ($E_p > 20$eV).

The symmetry of a crystal surface is immediately apparent by reference to the CID or LEED patterns. The precise structural determinations proceed by judiciously choosing, according to solid-state chemical principles, the atomic positions. The LEED intensities of the emergent beams are calculated as a function of primary-beam energy and compared with the experimental results. Adjustments to the atomic positions are then made, and the process is repeated. Thus, a structural determination can involve considerable computer time, making computational efficiency highly desirable.

RESULTS

The calculations of the following CID images were made using the Laboratory's mainframe computer and a Cray-1 computer located at Kirtland Air Force Base in New Mexico. Most of the source programs used in these computations are the LEED programs of Van Hove and Tong.[7]

Figure 4 shows the results of intensity calculations of the elastically backscattered electrons using the renormalized forward-scattering (RFS) perturbation theory along the three directions, as indicated in the inset. The inset also shows the position of the atoms in "real" space, along with the directions in the reciprocal lattice. To facilitate comparison of theory and experimental results, the total reflectivity was calculated as a function of the angle of incidence of the primary beam at 130 points, forming a grid in one octant of the (100) face of aluminum (Al). These calculations were done for a primary-beam energy of 6.55 hartrees (1 hartree = 27.2 eV) relative to the muffin-tin potential. The points in this octant were interpolated using cubic spline functions to a total of 1250 points for the octant. The theoretical CID image (Fig. 5) was created by assuming a linear-response function and using computer imaging methods. The contrast in this generated image has been reversed so that bright areas correspond to low reflectivities (i.e., they correspond to the experimental measurements). This image resembles the experimental CID image of Figure 1B taken
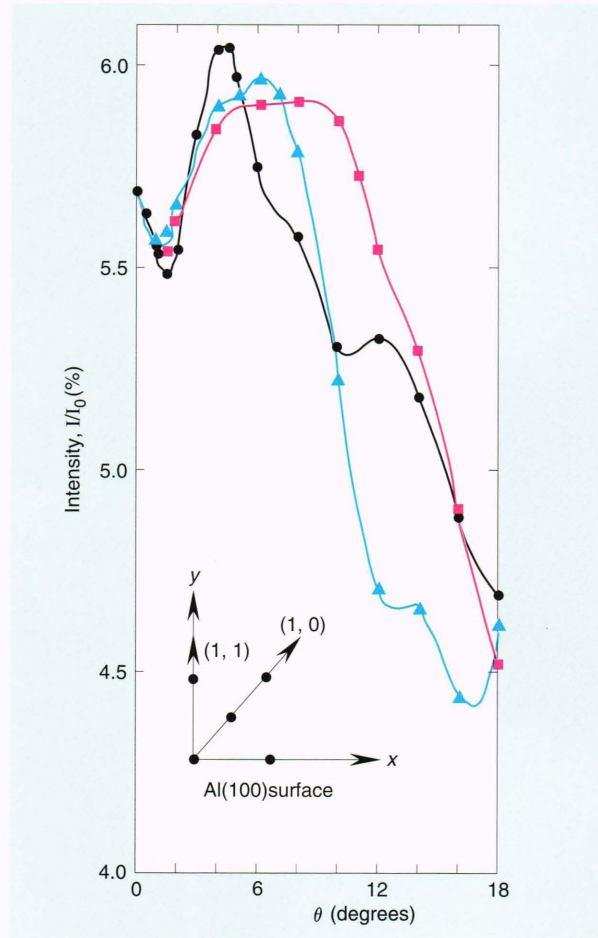

Figure 4. Theoretical elastically backscattered electron current for Al(100) as a function of angle of incidence along the (1, 1) direction of the reciprocal lattice (circles), the (1, 0) direction (circles and triangles), and midway between (squares). The primary-beam energy is 6.55 hartrees relative to the muffin-tin potential.

at 5.96 hartrees, suggesting, in turn, that the real part of the inner potential is 16 eV ([6.55 − 5.96] × 27.2). The largest discrepancy between theory and the experimental image is the large experimental reflectivity at the center ($\theta = 0°$), which theory predicts should be smaller and weaker. This difference can be attributed to the neglect of temperature effects in the theory and the energy-broadened primary electron beam, which would also explain the features in the experimental pattern being less sharp than expected from the theoretical image.

Figure 6 shows theoretical CID patterns as a function of the distance between the top two planes of atoms for the (111) surface of aluminum. These images exhibit the symmetry of the (111) surface[2] and indicate the sensitivity of the CID images to layer displacement. Temperature effects are included in the theoretical images. Close correlation seems to exist between the image at an interlayer spacing of 2.512 Å and the experimental image measured at 21 eV with respect to the vacuum (Fig. 1C). Theory and LEED experiments predict a slight relaxation outward of the first two layers for the Al(111) surface from the bulk spacing of 2.338 Å.
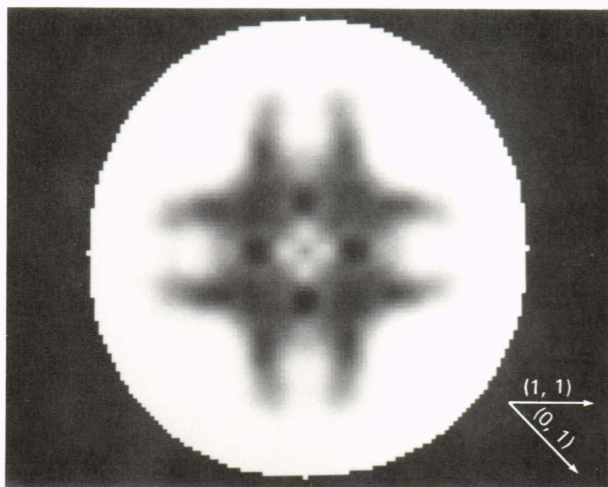
Figure 5. Theoretical image on the (100) aluminum surface for a primary-beam energy of 6.55 hartrees relative to the muffin-tin potential. High reflectivity is indicated by dark areas.
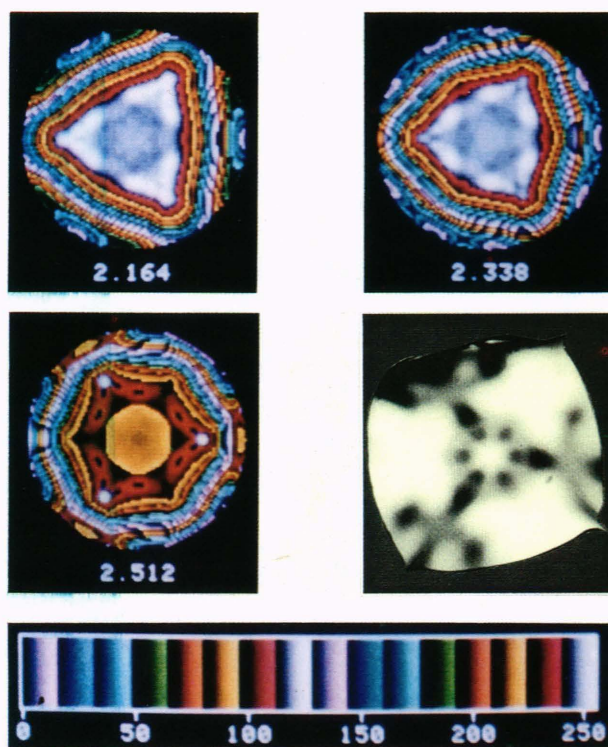
Figure 6. Theoretical current-image diffraction (CID) patterns of the (111) surface of aluminum calculated for an electron beam energy of 30 eV with respect to the vacuum for the indicated distances (in Å) between the surface layer and the second layer of atoms compared with an experimental CID image. The layer spacing of the bulk crystal is 2.338 Å. The relative intensity of reflected electrons is indicated by the color table at the bottom of the figure. The experimental image for this surface was measured at $E = 21$ eV with respect to the vacuum.

CONCLUSION

In this article, we have briefly outlined the calculations required to obtain theoretical CID images. Both the CID and LEED methods immediately give symmetry information about the particular surface under investigation; to obtain more detailed information requires extensive computations. The advantage of the CID method over that of LEED may be in the investigation of surface potential effects where the surface potential is responsible for the fine structure that appears in the CID images near the emergence condition for a new LEED beam.[6] When a diffracted beam starts to exit the crystal at near grazing angle, a portion of the beam is reflected from the surface barrier, is rediffracted from the first atomic layer back into the undiffracted or specular beam, and then exits the crystal. This phenomenon is manifested by sharp lines in the CID images.[6]

REFERENCES

[1] Nall, B. H., Jette, A. N., and Bargeron, C. B., "Diffraction Patterns in the Specimen-Current Images of a Single Crystal at Low Beam Energies," *Phys. Rev. Lett.* **48**, 882–885 (1982).
[2] Bargeron, C. B., Jette, A. N., and Nall, B. H., "Electron Current Image Diffraction from Crystal Surfaces at Low Energies," *Johns Hopkins APL Tech. Dig.* **5**, 51–55 (1984).
[3] Bargeron, C. B., Jette, A. N., and Nall, B. H., "Fine Structure in Two-Dimensional Electron Scattering," *Johns Hopkins APL Tech. Dig.* **11**, 180–181 (1990).
[4] Pendry, J. B., *Low Energy Electron Diffraction*, Academic Press, New York (1974).
[5] Abramowitz, M., and Stegun, I. A., *Handbook of Mathematical Functions*, National Bureau of Standards, Washington, D.C. (1964).
[6] Jette, A. N., Bargeron, C. B., and Nall, B. H., "Surface Potential Effects in Low-Energy Current Image Diffraction Patterns Observed on the Al(001) Surface," *J. Vac. Sci. Technol.* **A6**, 712–716 (1988).
[7] Van Hove, M. A., and Tong, S. Y., *Surface Crystallography by LEED*, Springer-Verlag, New York (1979).

THE AUTHORS

A. NORMAN JETTE received his Ph.D. in physics from the University of California, Riverside, in 1965. Dr. Jette joined APL that year and has worked in the Milton S. Eisenhower Research Center on theoretical problems in atomic, molecular, and solid-state physics. In 1972 he was visiting professor of physics at the Catholic University of Rio de Janeiro, Brazil, and in 1980 he was visiting scientist at the Center for Interdisciplinary Research at the University of Bielefeld, Federal Republic of Germany.

C. BRENT BARGERON earned a Ph.D. in physics at the University of Illinois in 1971 and joined APL that year as a member of the Research Center. Since then, Dr. Bargeron has been involved in problems in solid-state physics, light scattering, chemical lasers, arterial geometry, corneal damage from infrared radiation, mineral deposits in pathological tissues, quality control and failure analysis of microelectronic components, electron physics, and surface science.